MATERIALS SCIENCE

Unraveling electronic origins for boosting thermoelectric performance of p-type (Bi,Sb)$_2$Te$_3$

Rui Cheng[1]†, Haoran Ge[1]†, Shengpu Huang[2]†, Sen Xie[1], Qiwei Tong[1], Hao Sang[1], Fan Yan[1], Liangyu Zhu[1], Rui Wang[2], Yong Liu[3], Min Hong[4]*, Ctirad Uher[5], Qingjie Zhang[1], Wei Liu[1]*, Xinfeng Tang[1]*

P-type Bi$_{2-x}$Sb$_x$Te$_3$ compounds are crucial for thermoelectric applications at room temperature, with Bi$_{0.5}$Sb$_{1.5}$Te$_3$ demonstrating superior performance, attributed to its maximum density-of-states effective mass (m^*). However, the underlying electronic origin remains obscure, impeding further performance optimization. Herein, we synthesized high-quality Bi$_{2-x}$Sb$_x$Te$_3$ (00 *l*) films and performed comprehensive angle-resolved photoemission spectroscopy (ARPES) measurements and band structure calculations to shed light on the electronic structures. ARPES results directly evidenced that the band convergence along the $\overline{\Gamma}$-$\overline{M}$ direction contributes to the maximum m^* of Bi$_{0.5}$Sb$_{1.5}$Te$_3$. Moreover, strategic manipulation of intrinsic defects optimized the hole density of Bi$_{0.5}$Sb$_{1.5}$Te$_3$, allowing the extra valence band along $\overline{\Gamma}$-$\overline{K}$ to contribute to the electrical transport. The synergy of the above two aspects documented the electronic origins of the Bi$_{0.5}$Sb$_{1.5}$Te$_3$'s superior performance that resulted in an extraordinary power factor of ~5.5 milliwatts per meter per square kelvin. The study offers valuable guidance for further performance optimization of p-type Bi$_{2-x}$Sb$_x$Te$_3$.

INTRODUCTION

Thermoelectric (TE) technology enables the direct and reversible conversion between thermal and electrical energies and has emerged as a notable approach regarding environmentally friendly power generation and carbon emission reduction (*1*–*6*). The energy conversion efficiency of TE materials is determined by their dimensionless figure of merit $ZT = S^2\sigma T/\kappa$, where S stands for the Seebeck coefficient, σ is the electrical conductivity, T is the operating temperature, and κ is the total thermal conductivity that comprises both lattice (κ_{lat}) and electronic (κ_e) contributions (*7*–*11*). Boosting the power factor ($PF = S^2\sigma$) and ZT values of TE materials has long been considered a critical task for a more widespread use of thermoelectricity in various applications (*12*–*14*). The effort has focused on improving the existing TE materials while concurrently pioneering materials with high carrier mobility and low lattice thermal conductivity, particularly composed of low toxic and earth-abundant elements such as CaAl$_2$Si$_2$-type Zintl compounds (*15*, *16*), SnSe (*17*, *18*), and Ag$_2$Se (*19*) that were previously unidentified. Since being used for TE materials 70 years ago (*7*, *20*–*23*), Bi$_2$Te$_3$, Sb$_2$Te$_3$, Bi$_2$Se$_3$, and their alloys have maintained their dominant position for TE applications near room temperature. For example, Bi$_2$Te$_3$-based Peltier coolers are used for precise temperature control of optical modules in 5G communication systems (*24*, *25*), in polymerase chain reaction thermal cyclers (*26*, *27*), as well as in low-grade heat recovery and power generation, including self-powered wearable electronic devices (*28*–*32*). Of particular importance has been the high-performing p-type

Bi$_{0.5}$Sb$_{1.5}$Te$_3$ with its exceptional room-temperature power factor (PF) of 3.0 to 5.0 mW m^{-1} K^{-2} and ZT values of 1.0 to 1.8 (*33*–*38*), having its superior TE properties associated with the high density-of-states effective mass (m^*) (*39*, *40*).

Numerous theoretical and experimental studies were carried out to reveal the valence band structure of Bi$_{2-x}$Sb$_x$Te$_3$ that determines S, which can be expressed as $S \propto m^* \propto (N_V)^{2/3}m_b^*$, with N_V and m_b^* being the band degeneracy and single-valley effective mass, respectively (*41*–*45*). Density functional theory (DFT) calculations (*40*, *46*) have revealed that the valence band maximum (VBM) of Bi$_{2-x}$Sb$_x$Te$_3$ is not located at high-symmetry points of the Brillouin zone, and N_V and m^* thus acquire a high value. This could be well explained by the scenario of a topological electronic transition in Bi$_{2-x}$Sb$_x$Te$_3$, whereby strong spin-orbit interactions induce band inversion and gap opening, leading to the formation of complex conduction/valence band edges and the high N_V (*47*–*50*). DFT calculations corroborated the high N_V and the large m^* in p-type Bi$_{2-x}$Sb$_x$Te$_3$, but they could not explain the abrupt change in m^* and the largest values of m^* observed in p-type Bi$_{0.5}$Sb$_{1.5}$Te$_3$. Many attempts have been made to experimentally explore the underlying electronic origin responsible for the largest m^* observed in Bi$_{0.5}$Sb$_{1.5}$Te$_3$. First, investigations of the reflection spectra and electrical properties on single crystals of Bi$_{2-x}$Sb$_x$Te$_3$ have concluded that (*51*) the peak value of m^* in p-type Bi$_{0.5}$Sb$_{1.5}$Te$_3$ is due to a remarkable increase in the carrier pocket anisotropy and also the flattening of VBM. Second, assuming the valence band energy offset of Bi$_2$Te$_3$ being larger than that of Sb$_2$Te$_3$, Kim *et al.* (*52*) have recently put forward a reasonable hypothesis of valence band convergence to explain the abrupt change of m^* at Bi$_{0.5}$Sb$_{1.5}$Te$_3$. It should be noted that the two-valence band feature was previously proposed for both Bi$_2$Te$_3$ and Sb$_2$Te$_3$, with the calculated energy difference of 3.8 meV (*53*) and 27 meV (*54*) for Bi$_2$Te$_3$ and 4.9 meV (*54*) for Sb$_2$Te$_3$. Moreover, Shubnikov–de Haas measurements have indicated the valence bands energy offsets of ~15 and ~150 meV for Bi$_2$Te$_3$ and Sb$_2$Te$_3$, respectively (*55*, *56*). The reported two valence bands as well as the valence band energy offsets could not explain the hole pocket anisotropy nor the peak value of the effective mass m^* in Bi$_{0.5}$Sb$_{1.5}$Te$_3$. Therefore,

[1]State Key Laboratory of Advanced Technology for Materials Synthesis and Processing, Wuhan University of Technology, Wuhan 430070, China. [2]Institute for Structure and Function and Department of Physics, Chongqing University, Chongqing 400044, China. [3]School of Physics and Technology and The Key Laboratory of Artificial Micro/Nano Structures of Ministry of Education, Wuhan University, Wuhan 430072, China. [4]Centre for Future Materials, and School of Engineering, University of Southern Queensland, Springfield Central, Brisbane, Queensland 4300, Australia. [5]Department of Physics, University of Michigan, Ann Arbor, MI 48109, USA.
*Corresponding author. Email: w.liu@whut.edu.cn (W.L.); min.hong@unisq.edu.au (M.H.); tangxf@whut.edu.cn (X.T.).
†These authors contributed equally to this work.

the electronic origin for the abrupt change of $m*$ and the largest $m*$ in $Bi_{0.5}Sb_{1.5}Te_3$ among p-type $Bi_{2-x}Sb_xTe_3$ remained obscure, and this impeded any further improvement in the TE performance.

To address this issue, we epitaxially grew $Bi_{2-x}Sb_xTe_3$ (00 l) films with various Sb content using the molecular beam epitaxy (MBE) technique. We employed advanced characterization tools, including angle-resolved photoemission spectroscopy (ARPES) and scanning tunneling microscopy (STM), combined with band structure calculations and electrical transport measurements in this work. We systematically investigated the evolution of the valence band structure of $Bi_{2-x}Sb_xTe_3$ by varying the content of Sb. Moreover, we monitored the influence of intrinsic point defects and the Fermi level (E_F) position on the $m*$ of p-type $Bi_{0.5}Sb_{1.5}Te_3$. The results revealed that the ARPES-probed band convergence of the two valence bands along the $\overline{\Gamma}$-$\overline{M}$

direction together with the extra contribution from the valence band along the $\overline{\Gamma}$-$\overline{K}$ direction at a deep E_F were important electronic origins responsible for the largest $m*$ in $Bi_{0.5}Sb_{1.5}Te_3$ among all p-type $Bi_{2-x}Sb_xTe_3$. Furthermore, the record-high PF of 5.50 mW m^{-1} K^{-2} near-ambient temperature was obtained in the fabricated p-type $Bi_{0.5}Sb_{1.5}Te_3$ film under appropriate hole doping.

RESULTS

The valence band evolution of $Bi_{2-x}Sb_xTe_3$ with varying Sb content

Figure 1 illustrates the ARPES-obtained band structure and band-related properties of $Bi_{2-x}Sb_xTe_3$ (00 l) films with varying Sb content. All single-crystalline $Bi_{2-x}Sb_xTe_3$ ($x = 0$ to 2.0) films are epitaxially
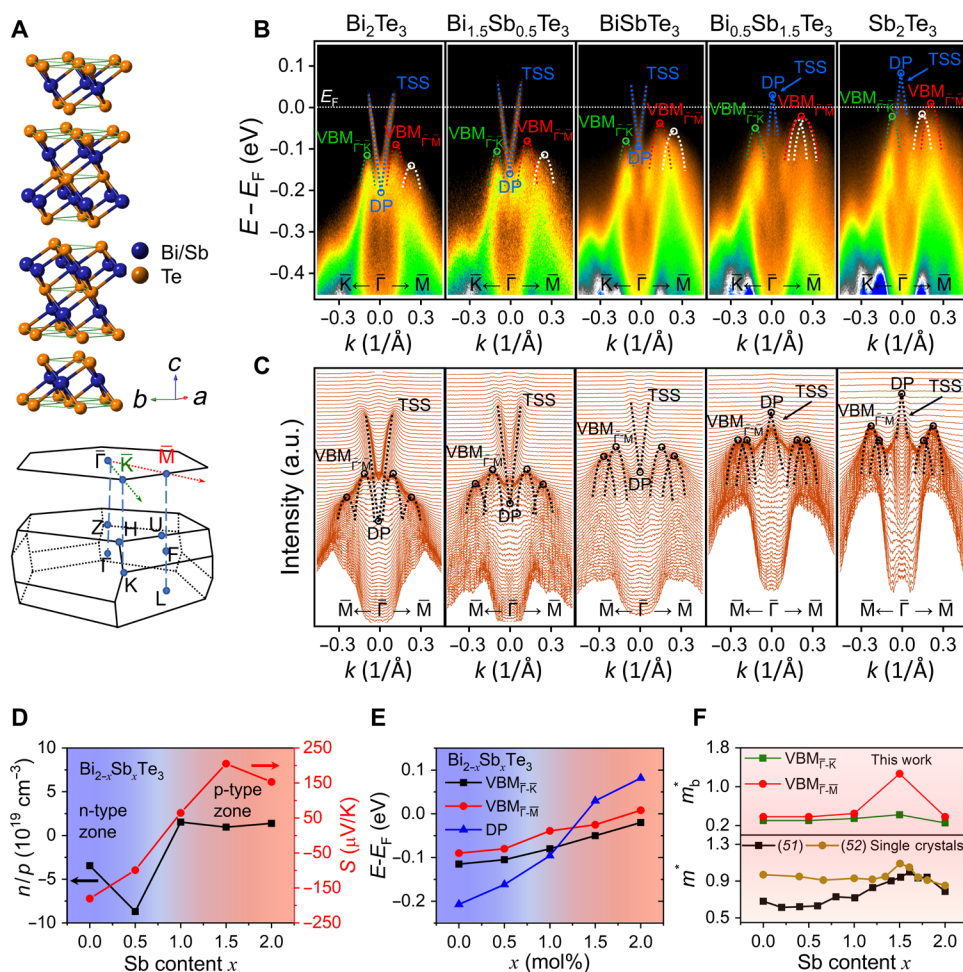

Fig. 1. ARPES band structures and band-related properties of $Bi_{2-x}Sb_xTe_3$. (**A**) Tetradymite-type crystal structure of $Bi_{2-x}Sb_xTe_3$ and the Brillouin zone with the high-symmetry points. $\overline{\Gamma}$-$\overline{K}$ and $\overline{\Gamma}$-$\overline{M}$ directions are denoted on the surface Brillouin zone. (**B**) ARPES intensity plots along $\overline{K}$-$\overline{\Gamma}$-$\overline{M}$ directions. E_F, TSS, DP, and VBM represent the Fermi level, the TSSs, the Dirac point, and the VBM, respectively. (**C**) The momentum distribution curves (MDCs) along the $\overline{\Gamma}$-$\overline{M}$ direction. Two valence bands are revealed by ARPES band dispersions along the $\overline{\Gamma}$-$\overline{M}$ direction, which are depicted by two downward parabolas (in black dashed lines) according to the MDC peak positions. Parabola fittings of the VBM along $\overline{\Gamma}$-$\overline{K}$ and $\overline{\Gamma}$-$\overline{M}$ directions in (B) are shown by green (VBM$_{\overline{\Gamma}-\overline{K}}$) and red (VBM$_{\overline{\Gamma}-\overline{M}}$) dashed curves, respectively, while the second valence band along the $\overline{\Gamma}$-$\overline{M}$ direction is marked by white dashed curves. Two valence bands along the $\overline{\Gamma}$-$\overline{M}$ direction align in energy at $Bi_{0.5}Sb_{1.5}Te_3$, resulting in the flattening of the red VBM$_{\overline{\Gamma}-\overline{M}}$ band. (**D**) The carrier density and Seebeck coefficient of $Bi_{2-x}Sb_xTe_3$ films as a function of Sb content x. As the x increases, the carrier transport switches from electron-dominated (n) to hole-dominated (p), while the transition appears at $x = 1.0$. (**E**) The energy positions of the topmost VBM$_{\overline{\Gamma}-\overline{K}}$ and VBM$_{\overline{\Gamma}-\overline{M}}$ bands as well as the DP as a function of Sb content x. The DP is displayed as the reference to determine the energy positions of VBMs. (**F**) The single valley effective mass (m_b^*) of VBM$_{\overline{\Gamma}-\overline{K}}$ and VBM$_{\overline{\Gamma}-\overline{M}}$ bands calculated from APRES (top) and the reported density-of-states effective mass ($m*$) (51, 52) derived from TE properties (bottom).

grown at a fixed substrate temperature (T_{sub}) of 533 K, with the phase structure and composition depicted in figs. S1 to S3. As schematically shown in Fig. 1A, carrier pockets (or electronic bands) in the Γ-Z-U-F-L and the Γ-Z-H-K planes are projected along the $\overline{\Gamma}\text{-}\overline{M}$ and $\overline{\Gamma}\text{-}\overline{K}$ directions of surface Brillouin zone, respectively. Figure 1B and figs. S4 and S5 show the ARPES intensity plots of $Bi_{2-x}Sb_xTe_3$ along different k paths. The topological surface states (TSS) with a linear band dispersion, the massless Dirac cone (DP) as well as the VBMs along the $\overline{\Gamma}\text{-}\overline{M}$ and $\overline{\Gamma}\text{-}\overline{K}$ directions, denoted as $VBM_{\overline{\Gamma}\text{-}\overline{M}}$ and $VBM_{\overline{\Gamma}\text{-}\overline{K}}$, are observed in the entire composition range of $Bi_{2-x}Sb_xTe_3$. These findings are also confirmed by our DFT calculations (see fig. S6) and align well with previous studies (47, 48, 57, 58). As shown in Fig. 1 (B and C), the E_F of $Bi_{2-x}Sb_xTe_3$ shifts remarkably toward the VBM with elevating the Sb content x, lastly entering the VBM at $x = 1.5$ and 2.0. This trend is also reflected in the evolution of the Fermi surface (FS) shown in fig. S7, where the predominating contribution gradually switches from the TSS to the VBM with the increase of x. Meanwhile, in the FS maps of films with $x = 1.5$ and 2.0, the ARPES intensity of $VBM_{\overline{\Gamma}\text{-}\overline{M}}$ band is distinctly higher than that of $VBM_{\overline{\Gamma}\text{-}\overline{K}}$ bands, as indicated by the brighter color in the former, highlighting the vital role of $VBM_{\overline{\Gamma}\text{-}\overline{M}}$ on their electronic transport properties. Figure 1D indicates a transition from n-type conduction (negative S and Hall coefficients) to p-type conduction (positive S and Hall coefficients) of fabricated $Bi_{2-x}Sb_xTe_3$ films, while the critical point of the transition occurs at $x = 1.0$. Other temperature-dependent electrical properties of $Bi_{2-x}Sb_xTe_3$ show a consistent evolution (fig. S8), agreeing with the variation trend of E_F and FS maps with the increasing content of Sb revealed by ARPES (Fig. 1, B and C, and fig. S7).

Sb alloying also induces a noticeable flattening of $VBM_{\overline{\Gamma}\text{-}\overline{M}}$ as well as a slight change in the energy difference between $VBM_{\overline{\Gamma}\text{-}\overline{M}}$ and $VBM_{\overline{\Gamma}\text{-}\overline{K}}$ for $Bi_{2-x}Sb_xTe_3$, as depicted by the curvatures of ARPES band dispersions in Fig. 1B. To comprehensively understand the band evolution of $Bi_{2-x}Sb_xTe_3$, we use the momentum distribution curves (MDCs) to trace the possible band dispersions from the MDC peak positions, shown in Fig. 1C and fig. S4B. $VBM_{\overline{\Gamma}\text{-}\overline{K}}$ MDCs of all $Bi_{2-x}Sb_xTe_3$ films can be well described as single bands (marked by green dashed curves), whereas the $VBM_{\overline{\Gamma}\text{-}\overline{M}}$ MDCs arise from two individual valence bands (denoted by red and white dashed curves). Such red and white bands move closer in energy with increasing the Sb content x, and the convergence of these two valence bands appears at $x = 1.5$ (schematically illustrated by two black dashed lines in Fig. 1C), providing a plausible explanation for the flattening of $VBM_{\overline{\Gamma}\text{-}\overline{M}}$.

The single valley effective mass (m_b^*) of VBM could be qualitatively estimated from the ARPES spectra by using the parabola fitting based on the equation $m_b^* = \hbar^2(\partial^2 E/\partial k^2)^{-1}$ (59, 60). Here, the energy position and the calculated m_b^* of the $VBM_{\overline{\Gamma}\text{-}\overline{K}}$ (the green band) and the topmost $VBM_{\overline{\Gamma}\text{-}\overline{M}}$ (the red band) of $Bi_{2-x}Sb_xTe_3$ are summarized in Fig. 1 (E and F, respectively). The energy of the red $VBM_{\overline{\Gamma}\text{-}\overline{M}}$ band is slightly higher than that of the green $VBM_{\overline{\Gamma}\text{-}\overline{K}}$ band with small energy offsets of 25 to 41 meV for all $Bi_{2-x}Sb_xTe_3$. Thus, the $VBM_{\overline{\Gamma}\text{-}\overline{M}}$ band substantially contributes to the electronic transport of p-type $Bi_{2-x}Sb_xTe_3$, while the $VBM_{\overline{\Gamma}\text{-}\overline{K}}$ band provides an additional contribution in the case of heavy hole doping. In addition, the m_b^* values of both the green $VBM_{\overline{\Gamma}\text{-}\overline{K}}$ band and the red $VBM_{\overline{\Gamma}\text{-}\overline{M}}$ band first increase and then decrease with increasing the Sb content x and peak at $x = 1.5$. It is important to note that the $Bi_{0.5}Sb_{1.5}Te_3$ acquires the abruptly increased m_b^* and the largest m_b^* of 1.27 m_e for $VBM_{\overline{\Gamma}\text{-}\overline{M}}$ among all p-type $Bi_{2-x}Sb_xTe_3$. This result agrees with reported m^* derived from TE properties, which shows that p-type $Bi_{0.5}Sb_{1.5}Te_3$

attains the largest m^* among p-type $Bi_{2-x}Sb_xTe_3$ (see the bottom panel of Fig. 1F) (51, 52). Therefore, our ARPES results validate that the presence of the abrupt change and the largest m^* at $Bi_{0.5}Sb_{1.5}Te_3$ could be ascribed to the convergence of two valence bands along the $\overline{\Gamma}\text{-}\overline{M}$ direction as well as the resulting abruptly increased m_b^*. Furthermore, the excellent PF obtained in p-type $Bi_{0.5}Sb_{1.5}Te_3$ could also come from the additional contribution from the green $VBM_{\overline{\Gamma}\text{-}\overline{K}}$ band under heavy hole doping, due to the small energy offset between $VBM_{\overline{\Gamma}\text{-}\overline{K}}$ and $VBM_{\overline{\Gamma}\text{-}\overline{M}}$.

The calculated band structures of $Bi_{2-x}Sb_xTe_3$ ($x = 0$ to 2.0) are displayed in Fig. 2 and fig. S9. The calculations reveal that the projections of high-lying valence bands along Z-H and Γ-K paths as well as along Z-U, Γ-F, and Γ-L paths form the $VBM_{\overline{\Gamma}\text{-}\overline{K}}$ and $VBM_{\overline{\Gamma}\text{-}\overline{M}}$, respectively. Noteworthy, valence bands from Γ-F and Γ-L paths can contribute to the $VBM_{\overline{\Gamma}\text{-}\overline{M}}$ of ternary $Bi_{2-x}Sb_xTe_3$. This is different from binary Bi_2Te_3 and Sb_2Te_3, where only the band from Z-U contributes to the $VBM_{\overline{\Gamma}\text{-}\overline{M}}$; see Fig. 2 (A to C). Thus, the band convergence of ARPES-probed two valence bands along the $\overline{\Gamma}\text{-}\overline{M}$ direction in ternary $Bi_{0.5}Sb_{1.5}Te_3$ is probably caused by two topmost valence bands projected from Z-U, Γ-F, and Γ-L paths. Inferred from molecular orbital theory (61) and topological electronic transition (7, 47), the band convergence of $Bi_{0.5}Sb_{1.5}Te_3$ might be promoted by altered orbital interactions (orbital overlap) as a result of the balance between bond polarity and spin-orbit coupling with varying Sb content. By setting the hole density (p) from 1×10^{19} to 2×10^{20} cm^{-3}, the calculated FS maps of p-type $Bi_{0.5}Sb_{1.5}Te_3$ evolves from the emergence of six-hole pockets (along six equivalent $\overline{\Gamma}\text{-}\overline{M}$ directions, representing $N_V = 6$) to a more complex "starfish" shape configuration, as shown in Fig. 2 (D to F). As elucidated in Fig. 2B, only valence bands along the $\overline{\Gamma}\text{-}\overline{M}$ direction contribute to the FS map in the case of light hole doping (marked by the red line, $p = 1 \times 10^{19}$ cm^{-3}), while multiple valence bands from both $\overline{\Gamma}\text{-}\overline{M}$ and $\overline{\Gamma}\text{-}\overline{K}$ directions contribute to the FS maps of p-type $Bi_{0.5}Sb_{1.5}Te_3$ under heavy hole doping (marked by the blue and black lines, $p \geq 1 \times 10^{20}$ cm^{-3}), resulting in the evolution of FS maps. The FS map of a $Bi_{0.5}Sb_{1.5}Te_3$ film in fig. S7 is generally similar to the result of Fig. 2D, suggesting that the as-grown $Bi_{0.5}Sb_{1.5}Te_3$ film in Fig. 1 is lightly hole doped. Both experiments and calculations in this work suggest that multiband transport and the increment of N_V are the primary reasons for the largest m^* [$m^* \propto (N_V)^{2/3} m_b^*$] and excellent PF of $Bi_{0.5}Sb_{1.5}Te_3$ among all p-type $Bi_{2-x}Sb_xTe_3$.

The optimization of E_F and the enhanced m^* and PF of p-type $Bi_{0.5}Sb_{1.5}Te_3$

To optimize the E_F and electrical transport of p-type $Bi_{0.5}Sb_{1.5}Te_3$, we fabricated a series of $Bi_{0.5}Sb_{1.5}Te_3$ films under various T_{sub} in the range of 533 to 613 K (referred to in Materials and Methods and figs. S10 and S11). Figure 3 displays the ARPES intensity plots and the FS maps of those $Bi_{0.5}Sb_{1.5}Te_3$ films, and figs. S12 and S13 show the MDCs. As shown in Fig. 3A, the E_F of $Bi_{0.5}Sb_{1.5}Te_3$ gradually shifts toward the VBM with the T_{sub} increasing from 533 to 613 K, while the E_F is close to the VBM, indicating the p-type conducting nature of fabricated films. The result suggests that increasing the T_{sub} can enhance p and deepen the E_F, which originates from the improved density of point defects contributing to free holes. Moreover, as the T_{sub} rises, the E_F crosses both $VBM_{\overline{\Gamma}\text{-}\overline{M}}$ and $VBM_{\overline{\Gamma}\text{-}\overline{K}}$, which brings forth two VBMs contributing to electrical transport and thus enhancing PF of fabricated $Bi_{0.5}Sb_{1.5}Te_3$ films. This conclusion is well supported by the evolution of ARPES-measured FS maps for

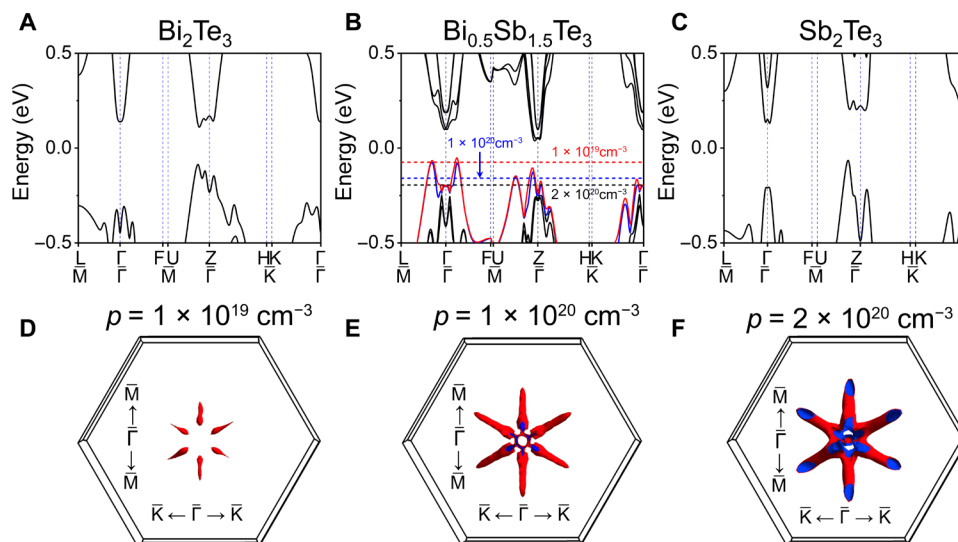**Fig. 2. DFT-calculated bulk band structure of Bi$_{2-x}$Sb$_x$Te$_3$.** Band structures along the high-symmetry directions for (**A**) Bi$_2$Te$_3$, (**B**) Bi$_{0.5}$Sb$_{1.5}$Te$_3$, and (**C**) Sb$_2$Te$_3$. The calculated valence band FSs of Bi$_{0.5}$Sb$_{1.5}$Te$_3$ under a given p: (**D**) $p = 1 \times 10^{19}$ cm^{-3}, (**E**) $p = 1 \times 10^{20}$ cm^{-3}, and (**F**) $p = 2 \times 10^{20}$ cm^{-3}, in which the Fermi level positions are indicated by red, blue, and black dashed lines in (B), respectively.
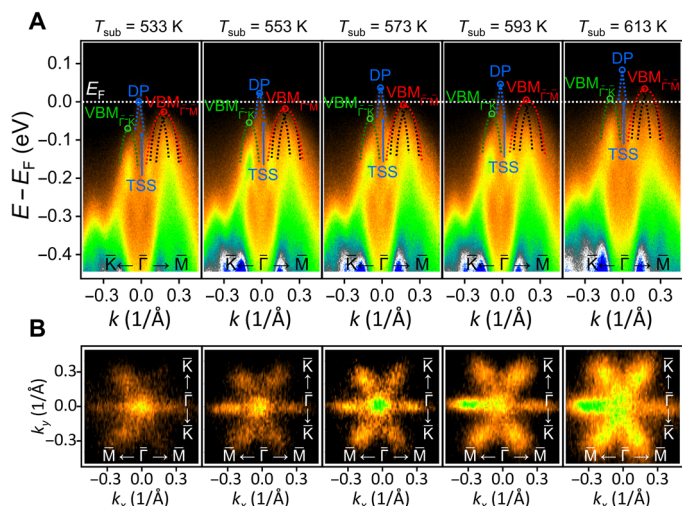

Fig. 3. ARPES band structures of Bi$_{0.5}$Sb$_{1.5}$Te$_3$ films fabricated with T_{sub} ranging from 533 K to 613 K. ARPES intensity plots along high-symmetry directions (**A**) and the corresponding FSs (**B**) for Bi$_{0.5}$Sb$_{1.5}$Te$_3$ films. E_F, TSS, and DP represent the Fermi level, the TSSs, and the Dirac point. VBM$_{\overline{\Gamma}-\overline{K}}$ and VBM$_{\overline{\Gamma}-\overline{M}}$ denote the topmost valence bands along $\overline{\Gamma}$-$\overline{K}$ and $\overline{\Gamma}$-$\overline{M}$ directions, respectively.

Bi$_{0.5}$Sb$_{1.5}$Te$_3$ films fabricated under various T_{sub}, as shown in Fig. 3B. First, the sizes of VBM$_{\overline{\Gamma}-\overline{M}}$ and VBM$_{\overline{\Gamma}-\overline{K}}$ band pockets increase markedly with the increasing T_{sub}, agreeing with the down-shift of E_F. Second, because the color contrast represents the spectra weight, the VBM$_{\overline{\Gamma}-\overline{K}}$ band pockets offer remarkably increasing contributions to the total spectral weight with the increasing T_{sub}. Moreover, the VBM$_{\overline{\Gamma}-\overline{K}}$ band will contribute substantially to the electronic transport of Bi$_{0.5}$Sb$_{1.5}$Te$_3$ films fabricated under $T_{sub} > 573$ K due to the noticeable spectra weight of VBM$_{\overline{\Gamma}-\overline{K}}$, coinciding with the changing trend in the calculated FS maps in Fig. 2 (D to F).

To identify the underlying mechanism behind the observed variation trend of E_F via tuning the T_{sub}, we performed atomically-resolved scanning tunneling microscope (STM) measurements on the fabricated Sb$_2$Te$_3$ and Bi$_{0.5}$Sb$_{1.5}$Te$_3$ films, as shown in Fig. 4. Previous calculations of defects and STM measurements have revealed (62–66) that the dominant intrinsic point defects in binary Sb$_2$Te$_3$ and Sb-rich Bi$_{2-x}$Sb$_x$Te$_3$ are antisite defects Sb$_{Te}$ (i.e., Sb atoms occupying the Te sites), due to their lowest formation energies among all intrinsic defects. In addition, antisite defects Te$_{Sb}$ (i.e., Te atoms occupying the Sb sites) and Sb vacancies (V$_{Sb}$) become the minority intrinsic defects, resulting from their higher formation energies. According to the STM surface morphologies of intrinsic defects reported by Jiang *et al.* (67) and Netsou *et al.* (68), four types of intrinsic defects (labeled I, II, III, and IV) are probed in our Sb$_2$Te$_3$ film and are distinguished from their characteristic surface morphologies for empty states (under positive bias) and filled states (under negative bias); see Fig. 4 (A to C). Defects I are donors as judged by the bright protrusions, while defects II to IV are acceptors due to the dark-depression feature of STM morphologies under positive bias, and vice versa. The donor feature and the triangular morphology suggest that defects I are antisite defects Te$_{Sb}$ located at the second atomic layer of a single Sb$_2$Te$_3$ quintuple layer. Using the same judgment, defects II and III are identified as antisite defects Sb$_{Te}$ that are situated at the first and fifth atomic layers, respectively, while defects IV are determined as Sb vacancies that are located at the fourth atomic layer, according to their characteristic STM morphologies. Figure 4D indicates that antisite defects Sb$_{Te}$ are dominant defects in Sb$_2$Te$_3$, which is judged from the highest density of Sb$_{Te}$ antisite defects (marked by white triangles) among all defects. Meanwhile, being fabricated at the same T_{sub} of 533 K, the Bi$_{0.5}$Sb$_{1.5}$Te$_3$ film contains much fewer Sb$_{Te}$ antisite defects as compared with that in the Sb$_2$Te$_3$ film, as depicted in Fig. 4 (D and E). The above result implies that the density of p-type Sb$_{Te}$ antisite defects increases with the increasing content of Sb, which explains the changing trend of E_F in Fig. 1B. Moreover,
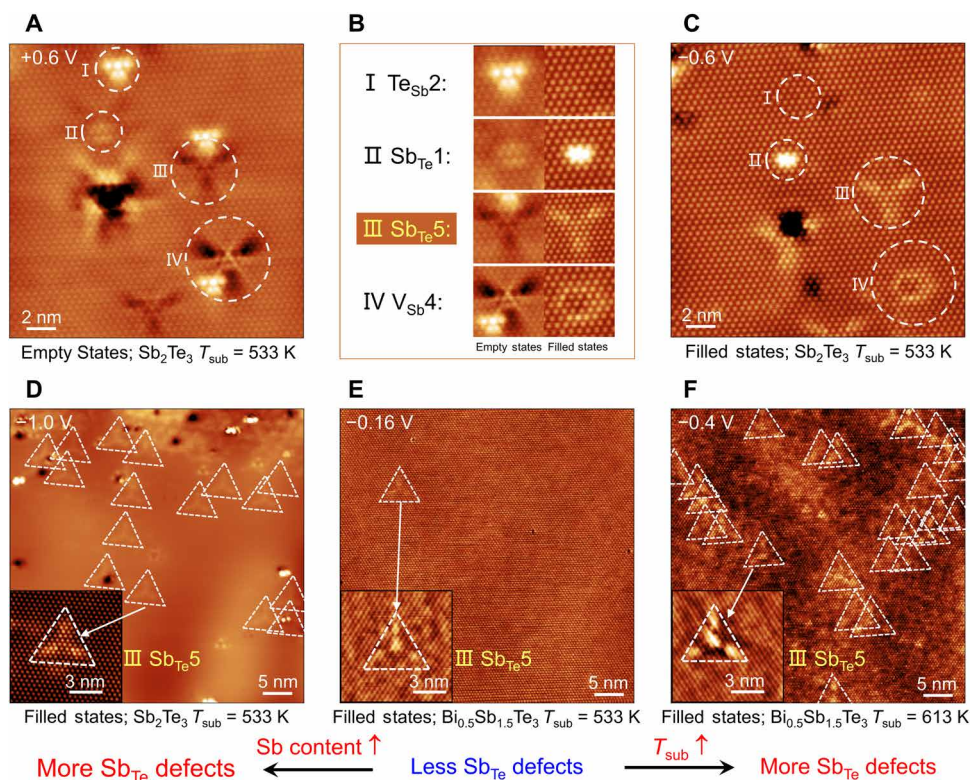
Fig. 4. Atomic-resolution STM surface morphologies of the fabricated Sb_2Te_3 and $Bi_{0.5}Sb_{1.5}Te_3$ films. Intrinsic point defects could be distinguished by their characteristic surface morphologies and the color contrast under positive bias (empty states) and negative bias (filled states). Four types of intrinsic point defects are found and marked by white circles shown in (**A** to **C**). (**D** to **F**) The defects of $Sb_{Te}5$, i.e., the Sb atoms occupying the Te sites at the fifth layer in a single Sb_2Te_3 quintuple layer, are the predominant defects in Sb_2Te_3 and $Bi_{0.5}Sb_{1.5}Te_3$ films, which are highlighted in inserted images and marked by white triangles. The numbers 1 to 5 denote the atomic layer number of the outmost Sb_2Te_3 and $Bi_{0.5}Sb_{1.5}Te_3$ quintuple layer.

the density of p-type Sb_{Te} antisite defects is significantly boosted in the $Bi_{0.5}Sb_{1.5}Te_3$ films with the T_{sub} rising from 533 to 578 K and to 613 K; see Fig. 4 (E and F) and fig. S14. The formation of Sb_{Te} antisite defects can be expressed by the following equation (*69*, *70*)

$$5V_{Te}^{\bullet\bullet} + 2Sb_{Sb} = (2V_{Sb}''' + 3V_{Te}^{\bullet\bullet}) + 2Sb_{Te}' + 12h^{\bullet} \tag{1}$$

in which the $V_{Te}^{\bullet\bullet}$, V_{Sb}''', and Sb_{Te}' represent the positively charged Te vacancies as well as the negatively charged Sb vacancies and Sb_{Te} antisite defects, respectively, while the $h^{\bullet}$ denotes a positively charged hole. Owing to the high vapor pressure of Te (*71*), a higher T_{sub} will cause a deficiency of Te and introduce more V_{Te}, thus favoring the formation of p-type Sb_{Te} antisite defects, which enhances the hole density p in $Bi_{0.5}Sb_{1.5}Te_3$ films. Therefore, the shift of the E_F toward VBM in p-type $Bi_{0.5}Sb_{1.5}Te_3$ films results from the generation of high density of p-type Sb_{Te} antisite defects through increasing the T_{sub}.

Figure 5 summarizes the electronic transport properties of fabricated $Bi_{0.5}Sb_{1.5}Te_3$ films under various T_{sub}. As shown in Fig. 5A, increasing T_{sub} notably increases the p of $Bi_{0.5}Sb_{1.5}Te_3$ films by over one order of magnitude. Specifically, the room-temperature p increases from 0.95×10^{19} cm^{-3} in the sample with $T_{sub} = 533$ K to 15.42×10^{19} cm^{-3} in the sample with $T_{sub} = 613$ K. This trend agrees with the E_F evolution revealed by ARPES and is ascribed to the dominating p-type Sb_{Te} antisite defects as aforementioned. As shown in Fig. 5B, the temperature dependence of the carrier mobility (μ) satisfies $\mu \propto T^{-3/2}$ near room temperature, indicating acoustic phonons as the dominating

carrier scattering mechanism in $Bi_{0.5}Sb_{1.5}Te_3$ films (*8*, *72*, *73*). Although the p increases more than one order of magnitude, the μ of $Bi_{0.5}Sb_{1.5}Te_3$ films declines slightly from 112 to 86 cm^2 V^{-1} s^{-1} at 300 K as the T_{sub} increases from 533 to 613 K. Consequently, with the rising T_{sub}, the electrical conductivity σ of the $Bi_{0.5}Sb_{1.5}Te_3$ film increases significantly, while the Seebeck coefficient S decreases gently (Fig. 5, C and D). The decrease of the temperature-dependent S is caused by the minor carrier excitation (*74–76*). The increase of p suppresses the minor carrier excitation in $Bi_{0.5}Sb_{1.5}Te_3$ films and shifts the peak of S toward high temperatures; see Fig. 5D. The turnover trend of S-T curves disappears in $Bi_{0.5}Sb_{1.5}Te_3$ films grown under $T_{sub} \geq 583$ K, confirming that the minor carrier excitation has been eliminated. Accordingly, the PF of $Bi_{0.5}Sb_{1.5}Te_3$ films is significantly boosted by increasing the T_{sub} and the p (Fig. 5E). The $Bi_{0.5}Sb_{1.5}Te_3$ film grown under $T_{sub} = 578$ K achieves the highest room temperature PF of 5.10 mW m^{-1} K^{-2} and the maximum PF (PF_{max}) of 5.50 mW m^{-1} K^{-2} at 323 K among all films, which is ensured by the optimized p of 7.25×10^{19} cm^{-3} at 300 K.

To further reveal the impact of valence band evolution on the m^*, we plot the correlation between S and p for fabricated $Bi_{0.5}Sb_{1.5}Te_3$ and Sb_2Te_3 films in Fig. 5F. The theoretical Pisarenko curves with different m^* are calculated by using the single parabolic band model (*77*, *78*) and are plotted in Fig. 5F. The electronic transport properties of fabricated Sb_2Te_3 films under different T_{sub} are shown in fig. S15. $Bi_{0.5}Sb_{1.5}Te_3$ films reach much higher S and m^* compared with Sb_2Te_3 films in a wide range of p, which is attributed to the convergence of
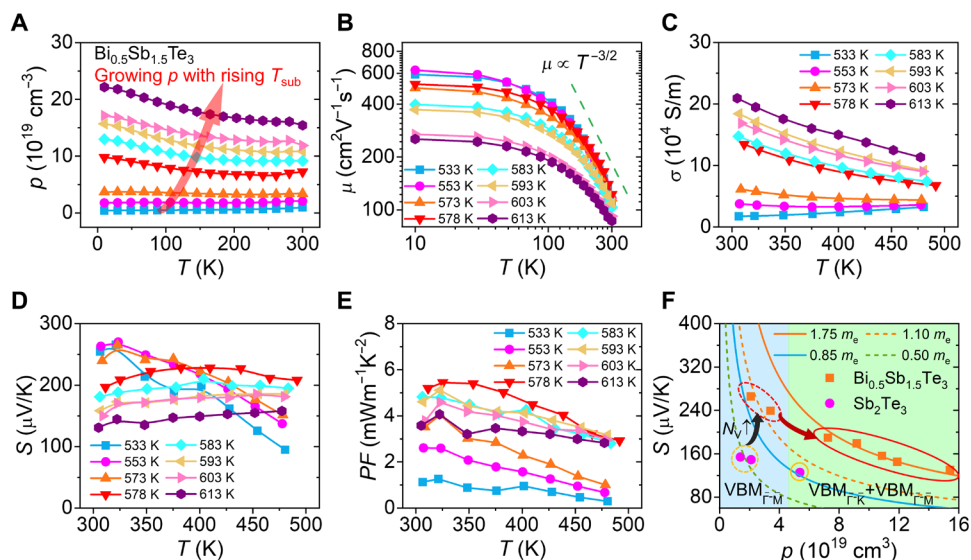
Fig. 5. The carrier transport and TE transport properties of Bi$_{0.5}$Sb$_{1.5}$Te$_3$ films fabricated at T_{sub} = 533 to 613 K. Temperature dependence of p (**A**), μ (**B**), σ (**C**), S (**D**), and PF (**E**). (**F**) The correlation between p and S. Four lines represent the theoretical Pisarenko curves with different m^*.

two valence bands along the $\overline{\Gamma}$-$\overline{M}$ direction as well as the increased N_V and m^* as already noted. Moreover, as the p increases, the m^* of Bi$_{0.5}$Sb$_{1.5}$Te$_3$ and Sb$_2$Te$_3$ are respectively increasing from 1.10 m_e and 0.50 m_e to 1.75 m_e and 0.85 m_e, verifying the additional contribution from the low-lying VBM$_{\overline{\Gamma}-\overline{M}}$ band when the films are heavily hole doped. Therefore, because of the optimized valence band structure, the PF_{max} obtained in the Bi$_{0.5}$Sb$_{1.5}$Te$_3$ film is significantly superior to the PF_{max} of 3.2 mW m^{-1} K^{-2} in Sb$_2$Te$_3$ films, as indicated in Fig. 5E and fig. S15F.

The two-step band structure optimization scheme for p-type Bi$_{2-x}$Sb$_x$Te$_3$

Figure 6A summarizes the found two-step band structure optimization for p-type Bi$_{2-x}$Sb$_x$Te$_3$. First, increasing Sb content shifts the E_F toward the valence band and induces the valence band convergence along the $\overline{\Gamma}$-$\overline{M}$ direction. As a result, Bi$_{0.5}$Sb$_{1.5}$Te$_3$ exhibits the maximum m^* among all p-type Bi$_{2-x}$Sb$_x$Te$_3$, as revealed in Figs. 1 and 2. Second, the higher T_{sub} facilitates the formation of Sb$_{Te}$ antisite defects, which moves the E_F deeper into the valence band, and enables the extra valence band along $\overline{\Gamma}$-$\overline{K}$ to participate in electrical transport. This leads to a further enhancement in m^* and p, as shown in Figs. 3 and 5. Hence, the composition-driven band convergence (the first step) and the E_F-induced contribution from an additional band (the second step) are at the heart of the remarkably high m^* and PF obtained in p-type Bi$_{0.5}$Sb$_{1.5}$Te$_3$. Figure 6B compares the PF_{max} of p-type Bi$_{2-x}$Sb$_x$Te$_3$ films reported in recent studies. The optimal composition of Bi$_{0.5}$Sb$_{1.5}$Te$_3$ results in the highest PF_{max} among all p-type Bi$_{2-x}$Sb$_x$Te$_3$ films. Notably, a record-high PF_{max} of 5.50 mW m^{-1} K^{-2} near-ambient temperature is obtained in our Bi$_{0.5}$Sb$_{1.5}$Te$_3$ film, significantly outperforming the reported PF_{max} of 1.2 ~ 4.5 mW m^{-1} K^{-2} (62, 79–87). Therefore, this study discloses the evolution of valence band structures of Bi$_{2-x}$Sb$_x$Te$_3$ when tuning the Sb content and the intrinsic point defects, as well as documents the record-high PF in the epitaxially grown p-type Bi$_{0.5}$Sb$_{1.5}$Te$_3$ film.

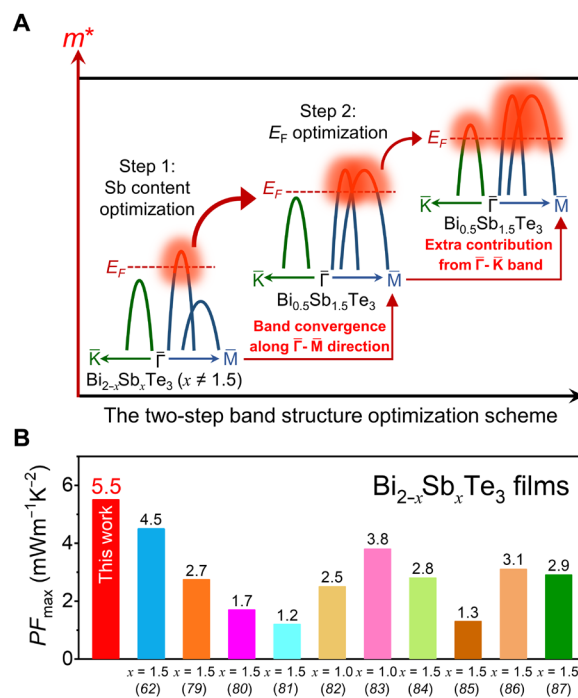**Fig. 6. The summary of valence band structure optimization leading to outstanding PF of Bi$_{0.5}$Sb$_{1.5}$Te$_3$.** (**A**) The two-step valence band structure optimization scheme. (**B**) The record-high PF of Bi$_{0.5}$Sb$_{1.5}$Te$_3$ film in this work and the comparison to literature reports.

DISCUSSION

In this study, we fabricate the high–crystalline quality Bi$_{2-x}$Sb$_x$Te$_3$ (00 l) films by MBE and investigate the influence of Sb content and intrinsic point defects on the valence band structure and TE performance. Through comprehensive ARPES measurements and band

structure calculations, we reveal the two-step band structure optimization scheme for p-type $Bi_{2-x}Sb_xTe_3$, addressing the long-standing challenge to understand the highest m^* attained in $Bi_{0.5}Sb_{1.5}Te_3$ among all p-type $Bi_{2-x}Sb_xTe_3$. We first consider the convergence of two valence bands along the $\overline{\Gamma}$-$\overline{M}$ direction in $Bi_{0.5}Sb_{1.5}Te_3$. We then show that both $VBM_{\overline{\Gamma}-\overline{M}}$ and $VBM_{\overline{\Gamma}-\overline{K}}$ bands contribute to the electronic transport of $Bi_{2-x}Sb_xTe_3$ under the condition of heavy hole doping due to the small energy offset between the two bands. STM measurements clarify that p-type Sb_{Te} antisites are the predominant defects and that, by increasing T_{sub}, the formation of Sb_{Te} antisites is promoted. Last, through the synergistic optimizations of the hole carrier density p and the valence band structure, the fabricated p-type $Bi_{0.5}Sb_{1.5}Te_3$ film with $p = 7.25 \times 10^{19}$ cm^{-3} (at 300 K) yields a record-high PF of 5.50 mW m^{-1} K^{-2} near-ambient temperature. This work substantially advances the understanding of the valence band structures of $Bi_{2-x}Sb_xTe_3$ and shows the road toward further improvements of the PF in p-type $Bi_{2-x}Sb_xTe_3$.

MATERIALS AND METHODS

Film fabrication

High-crystallinity $Bi_{2-x}Sb_xTe_3$ (00 l) films were epitaxially grown on Al_2O_3 (000 l) substrates in a commercial MBE system (Octoplus 300, Dr. Eberl MBE-Komponenten GmbH). High-purity Bi (99.9999%) and Sb_2Te_3 (99.999%) were evaporated from standard Knudsen cells, and Te (99.9999%) was evaporated from a special two-stage thermal cracker cell. The relative contents of Bi and Sb in $Bi_{2-x}Sb_xTe_3$ were modulated by adjusting the nominal flux ratios of Bi/Sb_2Te_3. During the growth process, in situ reflection high-energy electron diffraction was used for monitoring the phase structure of films. The film thickness was about 100 nm, measured by a step profiler (DektakXT, Bruker).

X-ray studies

The crystal structure was studied by a high-resolution x-ray diffraction (XRD) apparatus (smart lab, Rigaku), including the θ-2θ scan and rocking curve measurements. The actual composition and chemical states of constituent elements were determined by x-ray photoelectron spectroscopy (XPS; Scienta Omicron, XM1000), which is integrated into an MBE-STM-ARPES ultrahigh vacuum system. The content of Bi and Sb in $Bi_{2-x}Sb_xTe_3$ ($x = 0$ to 2.0) films was semiquantitatively determined on the basis of the ratio of XPS peak area for Bi-4f and Sb-3d core levels (88); see fig. S3 and table S1.

Band structure and point defects characterizations

The electronic band structure of fabricated $Bi_{2-x}Sb_xTe_3$ and $Bi_{0.5}Sb_{1.5}Te_3$ films was studied using the ARPES system (ARPES, Scienta Omicron) at 300 K. Monochromatic He−I ($h\nu = 21.2$ eV) light source and a state-of-the-art DA-30L hemispherical electron analyzer were used for measurements. Because of the thermal broadening at 300 K, the energy resolution is about 30 meV for all ARPES measurements, while the angle resolution is better than 0.2°. STM surface morphology measurements were performed in a scanning tunneling microscope (CreaTec Fisher & Co. GmbH) that operated at 77 K.

Electrical transport measurements

The Seebeck coefficient and electrical conductivity were measured simultaneously by commercial CTA-3 equipment in a helium atmosphere and at temperatures ranging from 300 to 473 K. The Hall coefficient (R_H) at low temperature (10 to 300 K) was measured by using a five-point configuration on a physical property measurement system (PPMS-9T, Quantum Design) with a magnetic field of ±1 T. The carrier concentration (n/p) and carrier mobility (μ) were calculated by $n(p) = 1/(e \cdot R_H)$ and $\mu = \sigma \cdot e \cdot |R_H|$.

DFT band structure calculations

The electronic band structures of $Bi_{2-x}Sb_xTe_3$ were computed through the application of DFT using the projector-augmented wave approach (89, 90), as implemented in the Vienna ab initio simulation package. Structural relaxation and electronic calculations were performed using the Perdew-Burke-Ernzerhof functional (91) with the generalized gradient approximation. To integrate over the Brillouin zone, an $11 \times 11 \times 11$ Monkhorst-Pack k-mesh was used, and the kinetic-energy cutoff was set to 550 eV. The atomic positions were optimized until the forces on each atom fell below 0.01 eV/Å. For the electronic self-consistent loop, the convergence criterion was set to 10^{-7} eV. The spin-orbit coupling effect and van der Waals interactions with the form of DFT-D3 (92) are considered throughout the calculation. To study the surface states, we used the iterative Green's function method, as implemented in the WANNIERTOOLS package. This method is based on maximally localized Wannier functions, which were constructed using wannier90 (93, 94).

Supplementary Materials

This PDF file includes:
Figs. S1 to S15
Table S1

REFERENCES AND NOTES

1. J. He, T. M. Tritt, Advances in thermoelectric materials research: Looking back and moving forward. *Science* **357**, eaak9997 (2017).
2. B. Jiang, W. Wang, S. Liu, Y. Wang, C. Wang, Y. Chen, L. Xie, M. Huang, J. He, High figure-of-merit and power generation in high-entropy GeTe-based thermoelectrics. *Science* **377**, 208–213 (2022).
3. D. Liu, D. Wang, T. Hong, Z. Wang, Y. Wang, Y. Qin, L. Su, T. Yang, X. Gao, Z. Ge, B. Qin, L.-D. Zhao, Lattice plainification advances highly effective SnSe crystalline thermoelectrics. *Science* **380**, 841–846 (2023).
4. Q. Yang, S. Yang, P. Qiu, L. Peng, T.-R. Wei, Z. Zhang, X. Shi, L. Chen, Flexible thermoelectrics based on ductile semiconductors. *Science* **377**, 854–858 (2022).
5. R. Venkatasubramanian, E. Siivola, T. Colpitts, B. O'quinn, Thin-film thermoelectric devices with high room-temperature figures of merit. *Nature* **413**, 597–602 (2001).
6. L. Xie, L. Yin, Y. Yu, G. Peng, S. Song, P. Ying, S. Cai, Y. Sun, W. Shi, H. Wu, N. Qu, F. Guo, W. Cai, H. Wu, Q. Zhang, K. Nielsch, Z. Ren, Z. Liu, J. Sui, Screening strategy for developing thermoelectric interface materials. *Science* **382**, 921–928 (2023).
7. X. Tang, Z. Li, W. Liu, Q. Zhang, C. Uher, A comprehensive review on Bi_2Te_3-based thin films: Thermoelectrics and beyond. *Interdiscip. Mater.* **1**, 88–115 (2022).
8. L. Chen, R. Liu, X. Shi, "Strategies to optimize thermoelectric performance" in *Thermoelectric Materials and Devices*, L. Chen, R. Liu, X. Shi, Eds. (Elsevier, 2021), pp. 19–50.
9. C. Liu, Z. Zhang, Y. Peng, F. Li, L. Miao, E. Nishibori, R. Chetty, X. Bai, R. Si, J. Gao, X. Wang, Y. Zhu, N. Wang, H. Wei, T. Mori, Charge transfer engineering to achieve extraordinary power generation in GeTe-based thermoelectric materials. *Sci. Adv.* **9**, eadh0713 (2023).
10. L. Xie, C. Ming, Q. Song, C. Wang, J. Liao, L. Wang, C. Zhu, F. Xu, Y.-Y. Sun, S. Bai, L. Chen, Lead-free and scalable GeTe-based thermoelectric module with an efficiency of 12%. *Sci. Adv.* **9**, eadg7919 (2023).
11. S. Roychowdhury, T. Ghosh, R. Arora, M. Samanta, L. Xie, N. K. Singh, A. Soni, J. He, U. V. Waghmare, K. Biswas, Enhanced atomic ordering leads to high thermoelectric performance in $AgSbTe_2$. *Science* **371**, 722–727 (2021).
12. G. Tan, L.-D. Zhao, M. G. Kanatzidis, Rationally designing high-performance bulk thermoelectric materials. *Chem. Rev.* **116**, 12123–12149 (2016).
13. X.-L. Shi, J. Zou, Z.-G. Chen, Advanced thermoelectric design: From materials and structures to devices. *Chem. Rev.* **120**, 7399–7515 (2020).
14. Y. Pei, H. Wang, G. J. Snyder, Band engineering of thermoelectric materials. *Adv. Mater.* **24**, 6125–6135 (2012).

15. J. Mao, H. Zhu, Z. Ding, Z. Liu, G. A. Gamage, G. Chen, Z. Ren, High thermoelectric cooling performance of n-type Mg_3Bi_2-based materials. *Science* **365**, 495–498 (2019).

16. J. Zhang, L. Song, G. K. H. Madsen, K. F. F. Fischer, W. Zhang, X. Shi, B. B. Iversen, Designing high-performance layered thermoelectric materials through orbital engineering. *Nat. Commun.* **7**, 10892 (2016).

17. B. Qin, L.-D. Zhao, Moving fast makes for better cooling. *Science* **378**, 832–833 (2022).

18. Y. Xiao, L.-D. Zhao, Seeking new, highly effective thermoelectrics. *Science* **367**, 1196–1197 (2020).

19. T.-R. Wei, P. Qiu, K. Zhao, X. Shi, L. Chen, Ag_2Q-Based (Q = S, Se, Te) silver chalcogenide thermoelectric materials. *Adv. Mater.* **35**, e2110236 (2023).

20. H. Goldsmid, R. Douglas, The use of semiconductors in thermoelectric refrigeration. *Br. J. Appl. Phys.* **5**, 386–390 (1954).

21. B. Poudel, Q. Hao, Y. Ma, Y. Lan, A. Minnich, B. Yu, X. Yan, D. Wang, A. Muto, D. Vashaee, X. Chen, J. Liu, M. S. Dresselhaus, G. Chen, Z. Ren, High-thermoelectric performance of nanostructured bismuth antimony telluride bulk alloys. *Science* **320**, 634–638 (2008).

22. B. Zhu, X. Liu, Q. Wang, Y. Qiu, Z. Shu, Z. Guo, Y. Tong, J. Cui, M. Gu, J. He, Realizing record high performance in n-type Bi_2Te_3-based thermoelectric materials. *Energ. Environ. Sci.* **13**, 2106–2114 (2020).

23. M. Hong, Z.-G. Chen, J. Zou, Fundamental and progress of Bi_2Te_3-based thermoelectric materials. *Chin. Phys.* B **27**, 048403 (2018).

24. D. Yang, Y. Xing, J. Wang, K. Hu, Y. Xiao, K. Tang, J. Lyu, J. Li, Y. Liu, P. Zhou, Y. Yu, Y. Yan, X. Tang, Multifactor roadmap for designing low-power-consumed micro thermoelectric thermostats in a closed-loop integrated 5G optical module. *Interdiscip. Mater.* **3**, 326–337 (2024).

25. I. Chowdhury, R. Prasher, K. Lofgreen, G. Chrysler, S. Narasimhan, R. Mahajan, D. Koester, R. Alley, R. Venkatasubramanian, On-chip cooling by superlattice-based thin-film thermoelectrics. *Nat. Nanotechnol.* **4**, 235–238 (2009).

26. Q. Zhang, K. Deng, L. Wilkens, H. Reith, K. Nielsch, Micro-thermoelectric devices. *Nat. Electron.* **5**, 333–347 (2022).

27. M. Amasia, M. Cozzens, M. J. Madou, Centrifugal microfluidic platform for rapid PCR amplification using integrated thermoelectric heating and ice-valving. *Sens. Actuators B Chem.* **161**, 1191–1197 (2012).

28. Z.-H. Zheng, X.-L. Shi, D.-W. Ao, W.-D. Liu, M. Li, L.-Z. Kou, Y.-X. Chen, F. Li, M. Wei, G.-X. Liang, P. Fan, G. Q. Lu, Z.-G. Chen, Harvesting waste heat with flexible Bi_2Te_3 thermoelectric thin film. *Nat. Sustain.* **6**, 180–191 (2023).

29. S. Yang, P. Qiu, L. Chen, X. Shi, Recent developments in flexible thermoelectric devices. *Small Sci.* **1**, 2100005 (2021).

30. L. Zhang, X.-L. Shi, Y.-L. Yang, Z.-G. Chen, Flexible thermoelectric materials and devices: From materials to applications. *Mater. Today* **46**, 62–108 (2021).

31. K. Kanahashi, J. Pu, T. Takenobu, 2D Materials for Large-Area Flexible Thermoelectric Devices. *Adv. Energy Mater.* **10**, 1902842 (2020).

32. Y. Lu, Y. Zhou, W. Wang, M. Hu, X. Huang, D. Mao, S. Huang, L. Xie, P. Lin, B. Jiang, B. Zhu, J. Feng, J. Shi, Q. Lou, Y. Huang, J. Yang, J. Li, G. Li, J. He, Staggered-layer-boosted flexible Bi_2Te_3 films with high thermoelectric performance. *Nat. Nanotechnol.* **18**, 1281–1288 (2023).

33. S. I. Kim, K. H. Lee, H. A. Mun, H. S. Kim, S. W. Hwang, J. W. Roh, D. J. Yang, W. H. Shin, X. S. Li, Y. H. Lee, Dense dislocation arrays embedded in grain boundaries for high-performance bulk thermoelectrics. *Science* **348**, 109–114 (2015).

34. R. Deng, X. Su, S. Hao, Z. Zheng, M. Zhang, H. Xie, W. Liu, Y. Yan, C. Wolverton, C. Uher, M. G. Kanatzidis, X. Tang, High thermoelectric performance in $Bi_{0.46}Sb_{1.54}Te_3$ nanostructured with ZnTe. *Energ. Environ. Sci.* **11**, 1520–1535 (2018).

35. W. Xie, J. He, H. J. Kang, X. Tang, S. Zhu, M. Laver, S. Wang, J. R. D. Copley, C. M. Brown, Q. Zhang, T. M. Tritt, Identifying the specific nanostructures responsible for the high thermoelectric performance of (Bi,Sb)$_2$Te$_3$ nanocomposites. *Nano Lett.* **10**, 3283–3289 (2010).

36. Y. Ma, Q. Hao, B. Poudel, Y. Lan, B. Yu, D. Wang, G. Chen, Z. Ren, Enhanced thermoelectric figure-of-merit in p-Type nanostructured bismuth antimony tellurium alloys made from elemental chunks. *Nano Lett.* **8**, 2580–2584 (2008).

37. L. Hu, T. Zhu, X. Liu, X. Zhao, Point Defect Engineering of High-Performance Bismuth-Telluride-Based Thermoelectric Materials. *Adv. Funct. Mater.* **24**, 5211–5218 (2014).

38. G. Zheng, X. Su, H. Xie, Y. Shu, T. Liang, X. She, W. Liu, Y. Yan, Q. Zhang, C. Uher, M. G. Kanatzidis, X. Tang, High thermoelectric performance of p-BiSbTe compounds prepared by ultra-fast thermally induced reaction. *Energ. Environ. Sci.* **10**, 2638–2652 (2017).

39. M. Stordeur, "Valence band structure and the thermoelectric figure-of-merit of (Bi$_{1-x}$Sb$_x$)$_2$Te$_3$ crystals" in *CRC Handbook of Thermoelectrics*, D. M. Rowe, Ed. (CRC Press, 2018), pp. 239–256.

40. J. P. Heremans, B. Wiendlocha, "Tetradymites: Bi_2Te_3-related materials" in *Materials Aspect of Thermoelectricity*, C. Uher, Ed. (CRC Press, 2016), pp. 53–108.

41. Y. Pei, X. Shi, A. LaLonde, H. Wang, L. Chen, G. J. Snyder, Convergence of electronic bands for high performance bulk thermoelectrics. *Nature* **473**, 66–69 (2011).

42. G. Tan, S. Hao, S. Cai, T. P. Bailey, Z. Luo, I. Hadar, C. Uher, V. P. Dravid, C. Wolverton, M. G. Kanatzidis, All-Scale Hierarchically Structured p-Type PbSe Alloys with High Thermoelectric Performance Enabled by Improved Band Degeneracy. *J. Am. Chem. Soc.* **141**, 4480–4486 (2019).

43. B. Qin, D. Wang, X. Liu, Y. Qin, J.-F. Dong, J. Luo, J.-W. Li, W. Liu, G. Tan, X. Tang, J.-F. Li, J. He, L.-D. Zhao, Power generation and thermoelectric cooling enabled by momentum and energy multiband alignments. *Science* **373**, 556–561 (2021).

44. Y. Tang, Z. M. Gibbs, L. A. Agapito, G. Li, H.-S. Kim, M. B. Nardelli, S. Curtarolo, G. J. Snyder, Convergence of multi-valley bands as the electronic origin of high thermoelectric performance in $CoSb_3$ skutterudites. *Nat. Mater.* **14**, 1223–1228 (2015).

45. W. Liu, X. Tan, K. Yin, H. Liu, X. Tang, J. Shi, Q. Zhang, C. Uher, Convergence of conduction bands as a means of enhancing thermoelectric performance of n-type $Mg_2Si_{1-x}Sn_x$ solid solutions. *Phys. Rev. Lett.* **108**, 166601 (2012).

46. T. Fang, X. Li, C. Hu, Q. Zhang, J. Yang, W. Zhang, X. Zhao, D. J. Singh, T. Zhu, Complex Band Structures and Lattice Dynamics of Bi_2Te_3-Based Compounds and Solid Solutions. *Adv. Funct. Mater.* **29**, 1900677 (2019).

47. H. Zhang, C.-X. Liu, X.-L. Qi, X. Dai, Z. Fang, S.-C. Zhang, Topological insulators in Bi_2Se_3, Bi_2Te_3 and Sb_2Te_3 with a single Dirac cone on the surface. *Nat. Phys.* **5**, 438–442 (2009).

48. D. Kong, Y. Chen, J. J. Cha, Q. Zhang, J. G. Analytis, K. Lai, Z. Liu, S. S. Hong, K. J. Koski, S.-K. Mo, Z. Hussain, I. R. Fisher, Z.-X. Shen, Y. Cui, Ambipolar field effect in the ternary topological insulator (Bi_xSb_{1-x})$_2$Te$_3$ by composition tuning. *Nat. Nanotechnol.* **6**, 705–709 (2011).

49. I. T. Witting, F. Ricci, T. C. Chasapis, G. Hautier, G. J. Snyder, The Thermoelectric Properties of n-Type Bismuth Telluride: Bismuth Selenide Alloys $Bi_2Te_{3-x}Se_x$. *Research* **2020**, 4361703 (2020).

50. M. Y. Toriyama, G. J. Snyder, Band inversion-driven warping and high valley degeneracy. *Cell Rep. Phys. Sci.* **4**, 101392 (2023).

51. M. Stordeur, M. Stölzer, H. Sobotta, V. Riede, Investigation of the valence band structure of thermoelectric ($Bi_{1-x}Sb_x$)$_2$Te$_3$ Single crystals. *Phys. Stat. Solidi B* **150**, 165–176 (1988).

52. H.-S. Kim, N. A. Heinz, Z. M. Gibbs, Y. Tang, S. D. Kang, G. J. Snyder, High thermoelectric performance in ($Bi_{0.25}Sb_{0.75}$)$_2$Te$_3$ due to band convergence and improved by carrier concentration control. *Mater. Today* **20**, 452–459 (2017).

53. S. J. Youn, A. J. Freeman, First-principles electronic structure and its relation to thermoelectric properties of Bi_2Te_3. *Phys. Rev. B* **63**, 085112 (2001).

54. G. Wang, T. Cagin, Electronic structure of the thermoelectric materials Bi_2Te_3 and Sb_2Te_3 from first-principles calculations. *Phys. Rev. B* **76**, 075201 (2007).

55. A. von Middendorff, G. Landwehr, Evidence for a second valence band in p-type Bi_2Te_3 from Magneto-Seebeck and Shubnikov-De Haas-data. *Solid State Commun.* **11**, 203–207 (1972).

56. A. von Middendorff, K. Dietrich, G. Landwehr, Shubnikov-de Haas effect in p-type Sb_2Te_3. *Solid State Commun.* **13**, 443–446 (1973).

57. J. Zhang, C.-Z. Chang, Z. Zhang, J. Wen, X. Feng, K. Li, M. Liu, K. He, L. Wang, X. Chen, Q.-K. Xue, X. Ma, Y. Wang, Band structure engineering in ($Bi_{1-x}Sb_x$)$_2$Te$_3$ ternary topological insulators. *Nat. Commun.* **2**, 574 (2011).

58. Y. L. Chen, J. G. Analytis, J.-H. Chu, Z. K. Liu, S.-K. Mo, X. L. Qi, H. J. Zhang, D. H. Lu, X. Dai, Z. Fang, S. C. Zhang, I. R. Fisher, Z. Hussain, Z.-X. Shen, Experimental realization of a three-dimensional topological insulator, Bi_2Te_3. *Science* **325**, 178–181 (2009).

59. J. Mao, J. Shuai, S. Song, Y. Wu, R. Dally, J. Zhou, Z. Liu, J. Sun, Q. Zhang, C. dela Cruz, S. Wilson, Y. Pei, D. J. Singh, G. Chen, C.-W. Chu, Z. Ren, Manipulation of ionized impurity scattering for achieving high thermoelectric performance in n-type Mg_3Sb_2-based materials. *Proc. Natl. Acad. Sci. U.S.A.* **114**, 10548–10553 (2017).

60. C. Fu, M. Yao, X. Chen, L. Z. Maulana, X. Li, J. Yang, K. Imasato, F. Zhu, G. Li, G. Auffermann, U. Burkhardt, W. Schnelle, J. Zhou, T. Zhu, X. Zhao, M. Shi, M. Dressel, A. V. Pronin, G. J. Snyder, C. Felser, Revealing the intrinsic electronic structure of 3D half-Heusler thermoelectric materials by angle-resolved photoemission spectroscopy. *Adv. Sci.* **7**, 1902409 (2020).

61. W. G. Zeier, A. Zevalkink, Z. M. Gibbs, G. Hautier, M. G. Kanatzidis, G. J. Snyder, Thinking like a chemist: Intuition in thermoelectric materials. *Angew. Chem. Int. Ed.* **55**, 6826–6841 (2016).

62. M. Tan, X. Shi, W. Liu, M. Li, Y. Wang, H. Li, Y. Deng, Z. Chen, Synergistic texturing and Bi/Sb-Te antisite doping secure high thermoelectric performance in $Bi_{0.5}Sb_{1.5}Te_3$-based thin films. *Adv. Energy Mater.* **11**, 2102578 (2021).

63. M. Zhang, W. Liu, C. Zhang, S. Xie, Z. Li, F. Hua, J. Luo, Z. Wang, W. Wang, F. Yan, Y. Cao, Y. Liu, Z. Wang, C. Uher, X. Tang, Identifying the manipulation of individual atomic-scale defects for boosting thermoelectric performances in artificially controlled Bi_2Te_3 films. *ACS Nano* **15**, 5706–5714 (2021).

64. D. West, Y. Y. Sun, H. Wang, J. Bang, S. B. Zhang, Native defects in second-generation topological insulators: Effect of spin-orbit interaction on Bi_2Se_3. *Phys. Rev. B* **86**, 121201 (2012).

65. G. Wang, X. Zhu, Y. Sun, Y. Li, T. Zhang, J. Wen, X. Chen, K. He, L. Wang, X. Ma, J. Jia, S. B. Zhang, Q. Xue, Topological insulator thin films of Bi_2Se_3 with controlled electronic structure. *Adv. Mater.* **23**, 2929–2932 (2011).

66. D. O. Scanlon, P. D. C. King, R. P. Singh, A. de la Torre, S. M. Walker, G. Balakrishnan, F. Baumberger, C. R. A. Catlow, Controlling Bulk conductivity in topological insulators: Key role of anti-site defects. *Adv. Mater.* **24**, 2154–2158 (2012).

67. Y. Jiang, Y. Y. Sun, M. Chen, Y. Wang, Z. Li, C. Song, K. He, L. Wang, X. Chen, Q.-K. Xue, X. Ma, S. B. Zhang, Fermi-level tuning of epitaxial Sb_2Te_3 thin films on graphene by regulating intrinsic defects and substrate transfer doping. *Phys. Rev. Lett.* **108**, 066809 (2012).

68. A.-M. Netsou, D. A. Muzychenko, H. Dausy, T. Chen, F. Song, K. Schouteden, M. J. Van Bael, C. Van Haesendonck, Identifying native point defects in the topological insulator Bi_2Te_3. *ACS Nano* **14**, 13172–13179 (2020).

69. T. Zhu, L. Hu, X. Zhao, J. He, New insights into intrinsic point defects in V_2VI_3 thermoelectric materials. *Adv. Sci.* **3**, 1600004 (2016).

70. M. Zhang, W. Liu, C. Zhang, J. Qiu, S. Xie, F. Hua, Y. Cao, Z. Li, H. Xie, C. Uher, X. Tang, Thickness-dependent electronic transport induced by *in situ* transformation of point defects in MBE-grown Bi_2Te_3 thin films. *Appl. Phys. Lett.* **117**, 153902 (2020).

71. C. L. Yaws, Ed., "Vapor pressure graphs for inorganic compounds and elements" in *Inorganic Compounds and Elements* (Gulf Professional Publishing, 1995), vol. 4 of *Handbook of Vapor Pressure*, pp. 1–343.

72. C. Hu, K. Xia, C. Fu, X. Zhao, T. Zhu, Carrier grain boundary scattering in thermoelectric materials. *Energ. Environ. Sci.* **15**, 1406–1422 (2022).

73. J. Shuai, J. Mao, S. Song, Q. Zhu, J. Sun, Y. Wang, R. He, J. Zhou, G. Chen, D. J. Singh, Tuning the carrier scattering mechanism to effectively improve the thermoelectric properties. *Energ. Environ. Sci.* **10**, 799–807 (2017).

74. H. J. Goldsmid, J. W. Sharp, Estimation of the thermal band gap of a semiconductor from seebeck measurements. *J. Electron. Mater.* **28**, 869–872 (1999).

75. Z. M. Gibbs, H.-S. Kim, H. Wang, G. J. Snyder, Band gap estimation from temperature dependent Seebeck measurement–Deviations from the $2e|S|_{max}T_{max}$ relation. *Appl. Phys. Lett.* **106**, 022112 (2015).

76. T. Xing, R. Liu, F. Hao, P. Qiu, D. Ren, X. Shi, L. Chen, Suppressed intrinsic excitation and enhanced thermoelectric performance in $Ag_xBi_{0.5}Sb_{1.5-x}Te_3$. *J. Mater. Chem. C* **5**, 12619–12628 (2017).

77. R. Cheng, S. Hao, J. Li, H. Bai, S. Xie, Y. Gong, W. Liu, J. Wu, G. Tan, X. Tang, Identifying the origins of high thermoelectric performance in group IIIA element doped PbS. *ACS Appl. Mater. Interfaces* **12**, 14203–14212 (2020).

78. X. Su, S. Hao, T. P. Bailey, S. Wang, I. Hadar, G. Tan, T.-B. Song, Q. Zhang, C. Uher, C. Wolverton, X. Tang, M. G. Kanatzidis, Weak electron phonon coupling and deep level impurity for high thermoelectric performance $Pb_{1-x}Ga_xTe$. *Adv. Energy Mater.* **8**, 1800659 (2018).

79. Y. Chen, X. Nie, C. Sun, S. Ke, W. Xu, Y. Zhao, W. Zhu, W. Zhao, Q. Zhang, Realizing high-performance BiSbTe magnetic flexible films *via* acceleration movement and hopping migration of carriers. *Adv. Funct. Mater.* **32**, 2111373 (2022).

80. I.-H. Kim, Electronic transport properties of the flash-evaporated p-type $Bi_{0.5}Sb_{1.5}Te_3$ thermoelectric thin films. *Mater. Lett.* **44**, 75–79 (2000).

81. D.-H. Kim, G.-H. Lee, O.-J. Kim, The influence of post-deposition annealing on thermoelectric properties of Bi–Sb–Te films prepared by sputtering. *Semicond. Sci. Technol.* **22**, 132–136 (2007).

82. H.-C. Chang, C.-H. Chen, Y.-K. Kuo, Great enhancements in the thermoelectric power factor of BiSbTe nanostructured films with well-ordered interfaces. *Nanoscale* **5**, 7017–7025 (2013).

83. M. Tan, Y. Hao, X. Ren, Improvement of thermoelectric properties in $(Bi_{0.5}Sb_{0.5})_2Te_3$ films of nanolayered pillar arrays. *J. Electron. Mater.* **43**, 3098–3104 (2014).

84. E. Symeou, M. Pervolaraki, C. N. Mihailescu, G. I. Athanasopoulos, C. Papageorgiou, T. Kyratsi, J. Giapintzakis, Thermoelectric properties of $Bi_{0.5}Sb_{1.5}Te_3$ thin films grown by pulsed laser deposition. *Appl. Surf. Sci.* **336**, 138–142 (2015).

85. L. Cao, Y. Deng, H. Gao, Y. Wang, X. Chen, Z. Zhu, Towards high refrigeration capability: The controllable structure of hierarchical $Bi_{0.5}Sb_{1.5}Te_3$ flakes on a metal electrode. *Phys. Chem. Chem. Phys.* **17**, 6809–6818 (2015).

86. T. Parashchuk, O. Kostyuk, L. Nykyruy, Z. Dashevsky, High thermoelectric performance of p-type $Bi_{0.5}Sb_{1.5}Te_3$ films on flexible substrate. *Mater. Chem. Phys.* **253**, 123427 (2020).

87. X. Han, Z. Zhang, Z. Liu, C. Xu, X. Lu, L. Sun, P. Jiang, Effects of thickness on thermoelectric properties of $Bi_{0.5}Sb_{1.5}Te_3$ thin films. *Appl. Nanosci.* **10**, 2375–2381 (2020).

88. F. A. Stevie, C. L. Donley, Introduction to X-ray photoelectron spectroscopy. *J. Vac. Sci. Technol. Vac. Surf. Films* **38**, 063204 (2020).

89. P. E. Blöchl, Projector augmented-wave method. *Phys. Rev. B* **50**, 17953–17979 (1994).

90. G. Kresse, D. Joubert, From ultrasoft pseudopotentials to the projector augmented-wave method. *Phys. Rev. B* **59**, 1758–1775 (1999).

91. J. P. Perdew, K. Burke, M. Ernzerhof, Generalized gradient approximation made simple. *Phys. Rev. Lett.* **77**, 3865–3868 (1996).

92. S. Grimme, J. Antony, S. Ehrlich, H. Krieg, A consistent and accurate ab initio parametrization of density functional dispersion correction (DFT-D) for the 94 elements H-Pu. *J. Chem. Phys.* **132**, 154104 (2010).

93. A. A. Mostofi, J. R. Yates, Y.-S. Lee, I. Souza, D. Vanderbilt, N. Marzari, wannier90A tool for obtaining maximally-localised Wannier functions. *Comput. Phys. Commun.* **178**, 685–699 (2008).

94. Q. Wu, S. Zhang, H.-F. Song, M. Troyer, A. A. Soluyanov, WannierTools: An open-source software package for novel topological materials. *Comput. Phys. Commun.* **224**, 405–416 (2018).